Journal of Materials Science: Materials in Electronics (2020) 31:2650–2656
https://doi.org/10.1007/s10854-019-02804-w

Effect of Nb–Sm co-doping on the ionic conductivity of $Li_7La_3Zr_2O_{12}$ electrolytes

Qixi Zhang[1] · Yali Luo[1] · Sainan Chen[1] · Jiahui Jiao[1] · Muyi Shen[1] · Han Chen[1] · Lucun Guo[1]

Received: 16 October 2019 / Accepted: 21 December 2019 / Published online: 8 January 2020

Abstract
Li-conducting oxide material $Li_7La_3Zr_2O_{12}$ is a promising solid electrolyte due to its relatively high conductivity. In this work, $Li_{7-x+y}La_3Zr_{2-x-y}Nb_xSm_yO_{12}$ ($0 \le x \le 0.4$, $0 \le y \le 0.1$) was prepared using a solid-state synthesis method, and the effects of Nb–Sm co-doping on the structure, microstructure, and conductivity of $Li_7La_3Zr_2O_{12}$ were investigated. Results showed that the co-doping of supervalent cation Nb and low-valent cation Sm was able to facilitate the formation of cubic garnet modification. The optimized composition $Li_{6.7}La_3Zr_{1.5}Nb_{0.4}Sm_{0.1}O_{12}$ showed the highest relative density at 94.3%, and reached the highest total conductivity of 1.06×10^{-3} S/cm at 30 °C, with the lowest activation energy of 0.39 eV. Based on SEM and above results, it can be found that the Nb–Sm co-doping can enhance sinterability and increase density, leading to lower impedance and higher conductivity. Although a small amount of impurity phase $LaNbO_4$ was observed in the XRD patterns, its overall influence on ionic conductivity was negligible.

1 Introduction

Rechargeable lithium ion batteries have been widely used in portable electronic devices due to their high energy density compared to other battery systems [1–3]. However, the practical application of lithium ion batteries is hindered by lithium dendrite growth during cycling when organic liquid electrolytes are used [4, 5]. Compared with liquid electrolytes, solid electrolytes have the advantages of being more thermally and chemically stable, safer, and less toxic [6–9]. Therefore, the transition from liquid to solid electrolytes has been a significant boost for the development of lithium ion batteries. Furthermore, the use of solid electrolytes gives opportunity to employ metallic lithium as the anode and thereby improving the energy density [10–12].

Among various solid electrolytes, the garnet-structured $Li_7La_3Zr_2O_{12}$ (LLZO) has been extensively studied for its relatively high ionic conductivity (4×10^{-4} S/cm) at room temperature, in addition to its stability with metallic lithium [13]. LLZO is reported to have two polymorphs: the tetragonal phase (space group $I4_1/acd$) and cubic phase (space group Ia-3d and I-43d) [14], of which cubic Ia-3d exhibits an ionic conductivity two orders of magnitude higher than the tetragonal phase. The ease of Li^+ diffusion in cubic Ia-3d garnets is attributed to the existence of three-dimensional interconnected channels of partially occupied Li^+ lattice sites [15].

From the thermodynamic point of view, cubic phase LLZO is unstable at room temperature and transforms into a tetragonal phase [16, 17]. Extensive investigations suggest that supervalent doping of W^{6+} [18], Ta^{5+} [5], and Nb^{5+} [19] at Zr sites can stabilize the cubic garnet, and also lead to creating additional vacancies at Li^+ sites, decreasing free energy and eventually resulting in higher Li^+ conductivity [20]. Low-valent cations such as Al^{3+} [21], Ga^{3+} [22], and Gd^{3+} [23] can compensate for low Li content generated from supervalent doping and facilitate the transport of lithium ions [24].

Previous studies indicate that LLZO co-doping with supervalent cation and low-valent cation can significantly improve ionic conductivity [8, 23]. Luo et al. [23] also demonstrate that the ionic conductivity of LLZO is remarkably enhanced to 9.86×10^{-4} S/cm by Nb–Gd co-doping on the Zr site. It is also reported that the cubic phase was stabilized at room temperature by the introduction of Nb and *Y*, and the total conductivity reaches 8.29×10^{-4} S/cm [23].

✉ Han Chen
nanjingchenhan@163.com

✉ Lucun Guo
lc-guo@163.com

[1] College of Materials Science and Engineering, Nanjing Tech University, No.30 Puzhu South Road, Nanjing 211816, Jiangsu, People's Republic of China

The aim of this article is to study the effects of supervalent cation Nb and low-valent cation Sm co-doping on the structure, microstructure, and conductivity of $Li_7La_3Zr_2O_{12}$, and the correlations among the chemical composition, relative density, amount of grain boundary, and ionic conductivity are further investigated.

2 Experimental section

Lithium garnet with nominal compositions of $Li_{7-x+y}La_3Zr_{2-x-y}Nb_xSm_yO_{12}$ $(0 \le x \le 0.4,\ 0 \le y \le 0.1)$ ceramics were synthesized through the conventional solid-state reaction method. Stoichiometric proportion of Li_2CO_3 (99.9%), La_2O_3 (99.99%), ZrO_2 (99%), Nb_2O_5 (99.99%), and Sm_2O_3 (99%) was weighted as raw materials. 10 wt% additional Li_2CO_3 was added to make up the lithium evaporation during sintering. La_2O_3 and Sm_2O_3 powders have been pre-fired at 1000 °C for 6 h. These precursor powders were mixed in alcohol and ball-milled for 12 h, and then dried at 85 °C in the air blowing thermostatic oven. The dried mixtures were ground into fine powders with a mortar and pestle, and then heated at 950 °C for 12 h to synthesize the LLZO powders. The calcined powders were reground for 24 h in 2-propanol. After drying, the powders were pressed into pellets with a diameter of 20 mm under 180 MPa. Then, the green pellets were surrounded by the mother powder and sintered at 1150 °C for 24 h in Al_2O_3 crucible to obtain cubic LLZO.

The relative density of the samples was measured by the Archimedes method. The crystal structures of the electrolyte ceramics were characterized obtained by X-ray diffraction (XRD, ARL X'TRA diffractometer, Swiss, Cu–Kα, $\lambda = 0.1542$ nm), with a measurement range of $2\theta = 10$–$70°$ and a step interval of 0.02°. The microstructure was characterized by scanning electron microscopy using backscattered electron (SEM-BSE, JEOL, JEM-6510, Tokyo, Japan). The ionic conductivity of the pellets was measured from 30 °C to 120 °C by AC impedance, using an electrochemical work station (CHI 760E, Shanghai, China) with the frequency range from 1 Hz to 10 MHz in air atmosphere. Before the conductivity test, both sides of the pellets were polished and painted with silver paste as Li-ion blocking electrodes. The electronic conductivity was tested by potentiostatic polarization on an electrochemical work station with scanning time of 4000 s and applied voltage of 0.1 V at 30 °C.

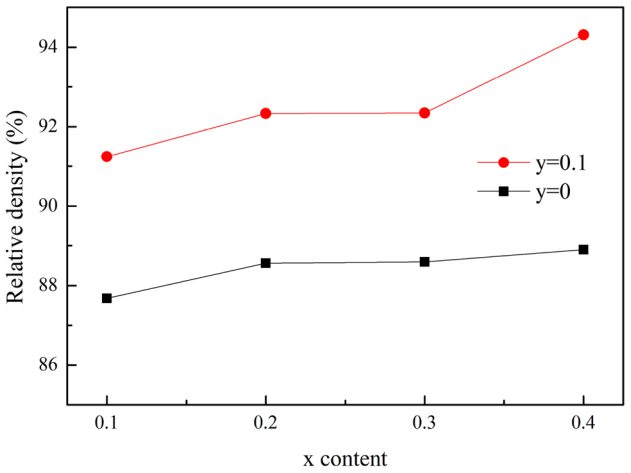

Fig. 1 The relative density of $Li_{7-x+y}La_3Zr_{2-x-y}Nb_xSm_yO_{12}$ varies with x and y contents

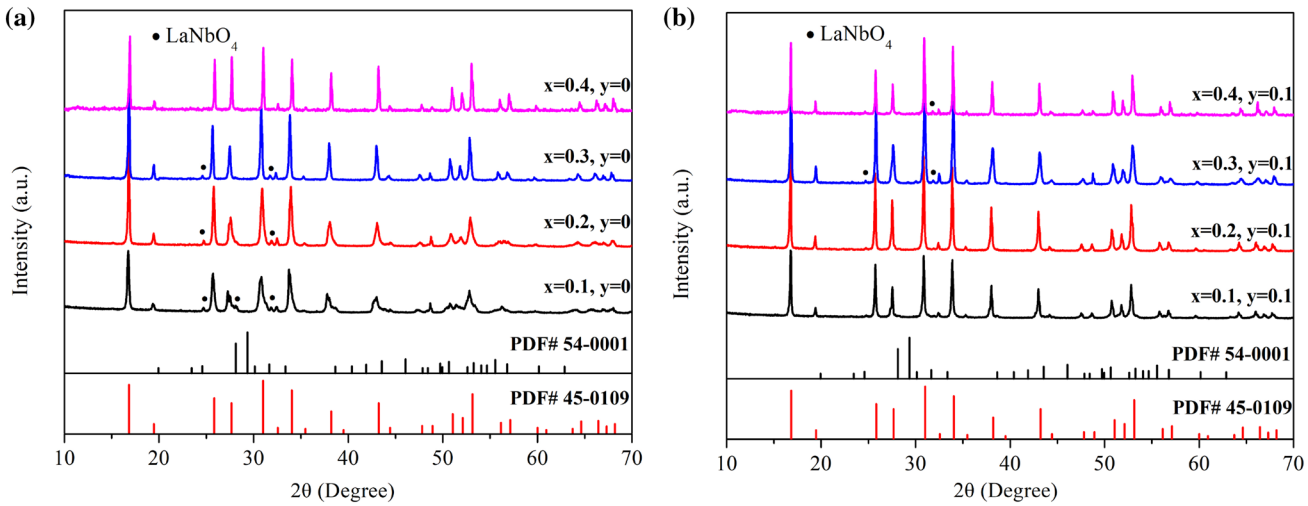

Fig. 2 XRD patterns for $Li_{7-x+y}La_3Zr_{2-x-y}Nb_xSm_yO_{12}$ ceramics sintered at 1150 °C for 24 h, **a** $x = 0.1$–0.4, $y = 0$; **b** $x = 0.1$–0.4, $y = 0.1$

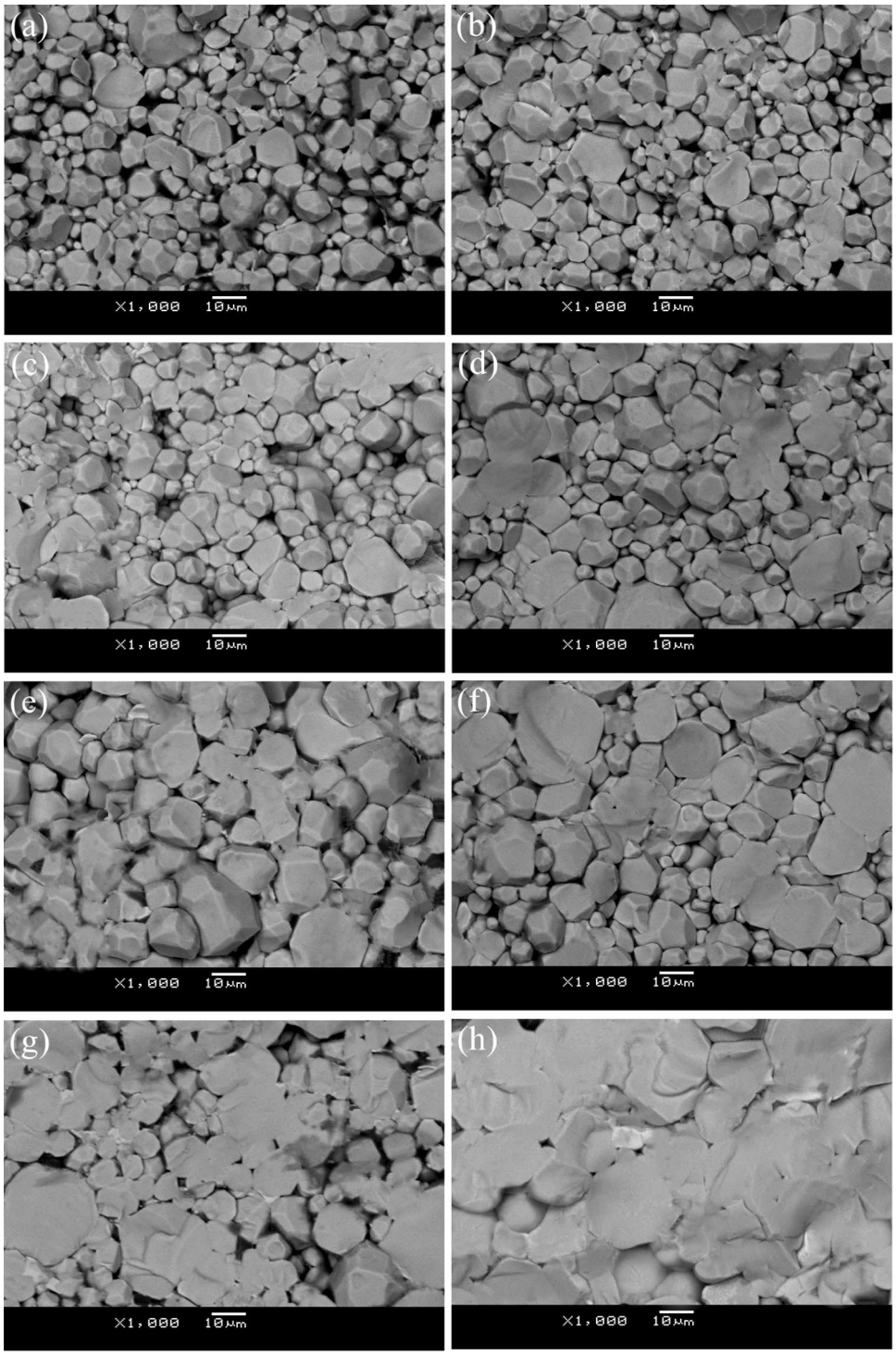

Fig. 3 SEM-BSE images of fractured cross section for $Li_{7-x+y}La_3Zr_{2-x-y}Nb_xSm_yO_{12}$ samples, **a**–**d** $x=0.1$–0.4, $y=0$; **e**–**h** $x=0.1$–0.4, $y=0.1$

3 Results and discussion

3.1 Sinterability

The density of the samples was measured by the Archimedes method using deionized water as medium. The experimental density ρ_e of the samples was derived from the equation given below:

$$\rho_{\text{experimental}} = \left(m_{\text{air}} / \left(m_{\text{air}} - m_{\text{water}}\right)\right) \times \rho_{\text{water}}, \quad (1)$$

Table 1 Average grain size measured by JEOL Smile View software from SEM images

Sample	Average powder/grain size (μm)	Standard deviation
$x=0.1, y=0$	6.03	2.25
$x=0.2, y=0$	7.55	1.75
$x=0.3, y=0$	8.59	2.27
$x=0.4, y=0$	9.54	2.51
$x=0.1, y=0.1$	8.70	1.70
$x=0.2, y=0.1$	9.85	2.84
$x=0.3, y=0.1$	10.90	2.97
$x=0.4, y=0.1$	18.36	2.83

where m_{air} is the weight of the sample in air (g), m_{water} is the weight of the sample in deionized water (g), and ρ_{water} is the density of deionized water (g/cm^3).

Theoretical density $\rho_{theoretical}$ can be calculated from the lattice parameters determined by XRD. So the relative density $\rho_{relative}$ can be calculated using the formula:

$$\rho_{relative} = \rho_{experimental} / \rho_{theoretical} \times 100\%. \quad (2)$$

Figure 1 shows the effects of doping amount on the relative density. Although the curve shows a tendency to increasing for the Nb-doped samples, the relative density did not change significantly, ranging from 87.68 to 88.97%. The relative density of the co-doping samples is obviously higher than the samples that only doped with Nb, and among all of the samples, $Li_{6.7}La_3Zr_{1.5}Nb_{0.4}Sm_{0.1}O_{12}$ shows the highest relative density at 94.31%.

3.2 Crystal structure and microstructure

Figure 2 presents the XRD patterns of $Li_{7-x+y}La_3Zr_{2-x-y}Nb_xSm_yO_{12}$ ($0 \le x \le 0.4$, $0 \le y \le 0.1$) ceramics sintered at 1150 °C for 24 h. Clearly, all diffraction peaks are assigned well to a cubic garnet-type structure (PDF #45-0109) with the space group Ia-3d, indicating that all the samples are basically cubic garnet-type oxides after calcination. The Nb–Sm co-doping is also shown to stabilize the cubic LLZO phase at room temperature. As for XRD patterns, some small shoulders corresponding to the impurity phase $LaNbO_4$ (PDF #54-0001) can be observed. It is interesting that in the Nb-doped samples, the impurity phase disappears with the increase of Nb content; however, in the co-doping samples, the impurity peaks appears with the increase of Nb content. The reason for this phenomenon is unclear, though comparing the relationship between XRD results and conductivity, it can be found that the effect of impurities on conductivity is very limited and almost negligible.

Figure 3 shows the cross-sectional SEM-BSE images of $Li_{7-x+y}La_3Zr_{2-x-y}Nb_xSm_yO_{12}$ ($0 \le x \le 0.4$, $0 \le y \le 0.1$)

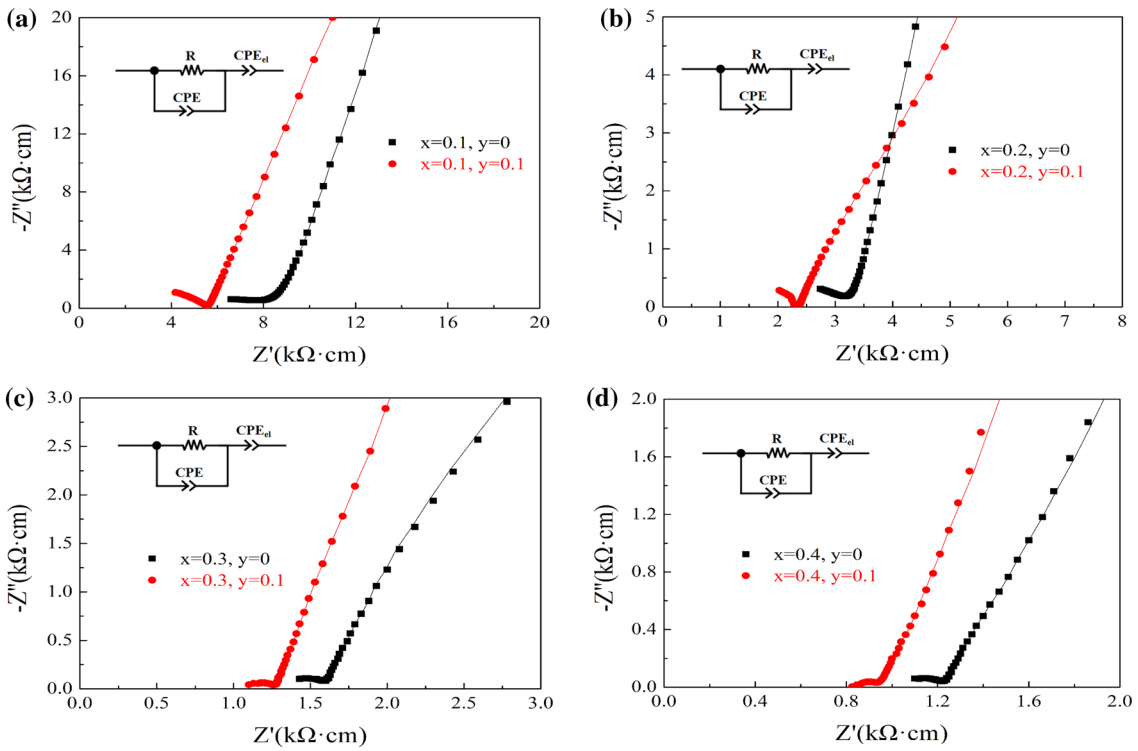

Fig. 4 AC impedance spectra of $Li_{7-x+y}La_3Zr_{2-x-y}Nb_xSm_yO_{12}$ ($0 \le x \le 0.4$, $0 \le y \le 0.1$) ceramic electrolytes at 30 °C

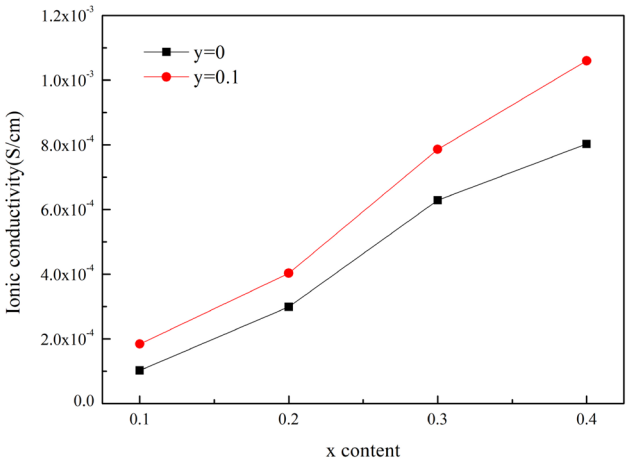

Fig. 5 Ionic conductivity varies with x content for $Li_{7-x+y}La_3Zr_{2-x-y}Nb_xSm_yO_{12}$ ($0 \le x \le 0.4$, $0 \le y \le 0.1$) samples

ceramics. The average grain size measured by JEOL Smile View software from SEM images is shown in Table 1. A large number of pores can be clearly observed due to incomplete intergranular contact in the samples that doped only with Nb (Fig. 3a–d). While it also can be seen that for the Nb–Sm co-doping samples, grains growth obviously (Fig. 3f–h). With the increase of Nb content, the amount of the pores decreases and the sample becomes more dense, in agreement with relative density results shown in Fig. 1. The correlation between grain structures and conductivity will be discussed further below.

3.3 Conductivity

Figure 4 presents the AC impedance spectra of $Li_{7-x+y}La_3Zr_{2-x-y}Nb_xSm_yO_{12}$ ($0 \le x \le 0.4$, $0 \le y \le 0.1$) ceramic electrolytes at 30 °C. All the spectra are composed of a depressed semicircle and a straight line. There is only

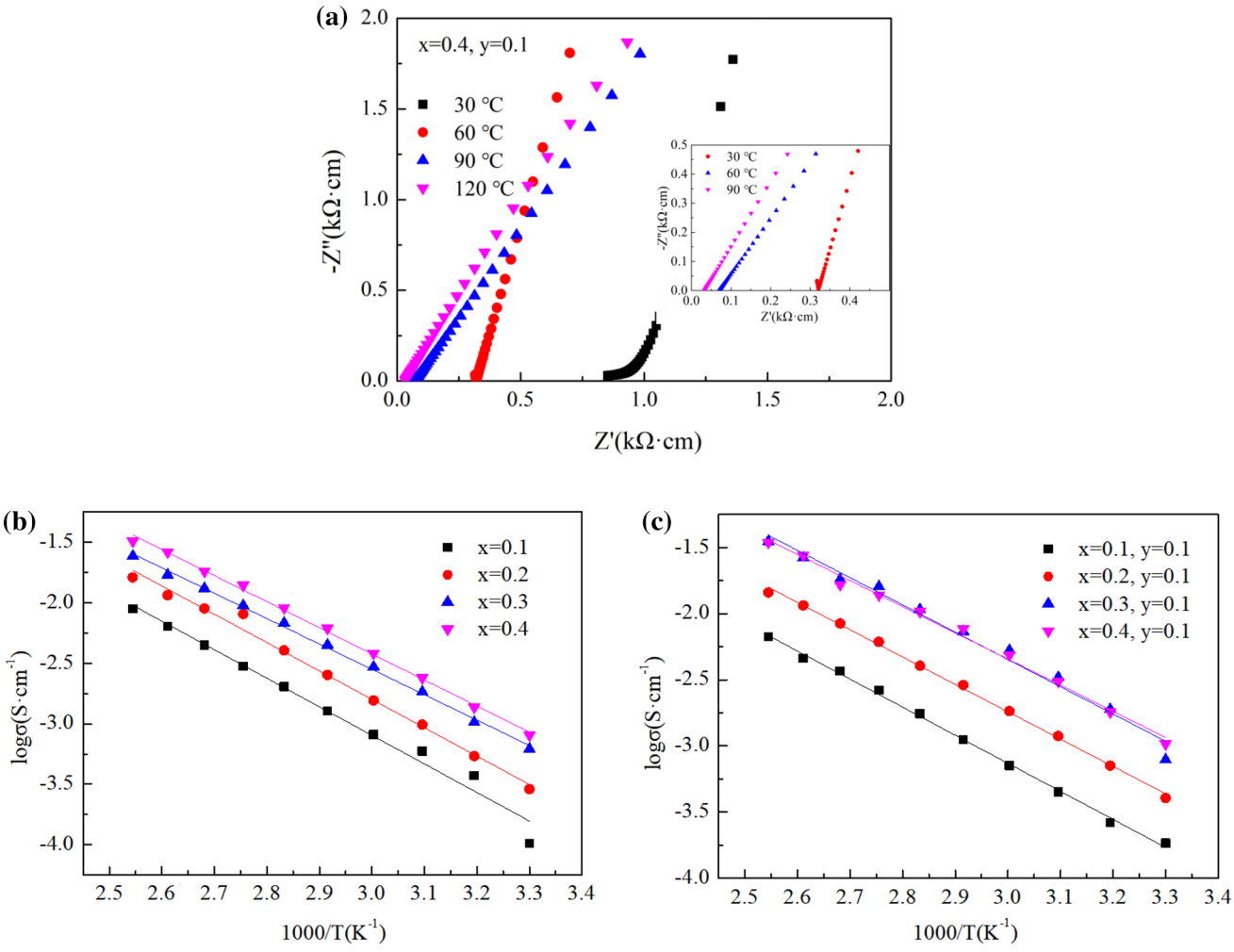

Fig. 6 **a** Nyquist plot of $Li_{6.7}La_3Zr_{1.5}N_{b0.4}Sm_{0.1}O_{12}$ with temperatures ranging from 30 to 120 °C. **b** Arrhenius plots of $Li_{7-x}La_3Zr_{2-x}Nb_xO_{12}$ ($0 \le x \le 0.4$). **c** Arrhenius plots of $Li_{7-x+y}La_3Zr_{2-x-y}Nb_xSm_yO_{12}$ ($0 \le x \le 0.4$, $0 \le y \le 0.1$)

Table 2 Electrochemical properties of $Li_{7-x+y}La_3Zr_{2-x-y}Nb_xSm_yO_{12}$ ($0 \le x \le 0.4$, $0 \le y \le 0.1$)

Sample	Ionic conductivity (S/cm)	Electronic conductivity (S/cm)	Activity energy (eV)
$x=0.1$, $y=0$	1.02×10^{-4}	1.34×10^{-8}	0.47
$x=0.2$, $y=0$	2.99×10^{-4}	6.32×10^{-9}	0.47
$x=0.3$, $y=0$	6.29×10^{-4}	4.23×10^{-10}	0.42
$x=0.4$, $y=0$	8.03×10^{-4}	7.36×10^{-9}	0.43
$x=0.1$, $y=0.1$	1.84×10^{-4}	2.38×10^{-8}	0.42
$x=0.2$, $y=0.1$	4.03×10^{-4}	1.42×10^{-8}	0.41
$x=0.3$, $y=0.1$	7.86×10^{-4}	3.33×10^{-9}	0.41
$x=0.4$, $y=0.1$	1.06×10^{-3}	8.60×10^{-10}	0.39

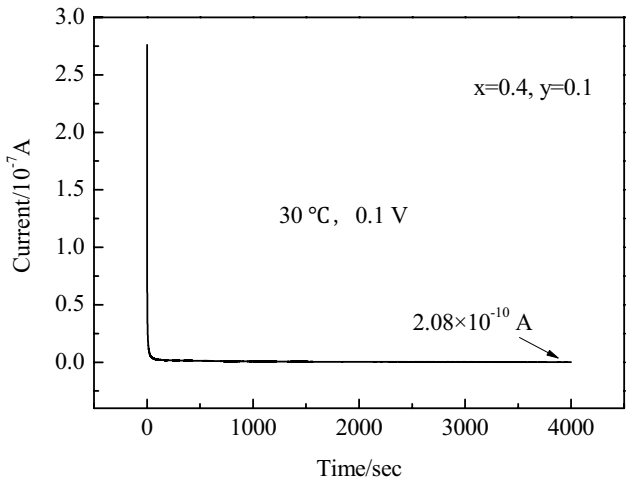

Fig. 7 DC potentiostatic polarization currents for $Li_{6.7}La_3Zr_{1.5}Nb_{0.4}Sm_{0.1}O_{12}$

one semicircle observed in the high-frequency region instead of two; therefore, it is difficult to separate grain and grain boundary contributions from the impedance spectra [25]. The ionic conductivity is calculated from the impedance data by fitting with a suitable equivalent circuit of (RCPE)(CPE_{el}), where R is the resistance, CPE is the constant phase element, and the subscript el refers to the electrode. The total conductivity of electrolytes can be expressed by $\sigma_{total}=L/RA$, where A is the area and L is the thickness of samples. The intercept point of the high-frequency semicircle can be represented by RA/L, and total conductivity can be calculated by the inverse of RA/L. Figure 5 shows the ionic conductivity varies with x content for the samples, which is derived from Fig. 4; it can be found that compared to the samples that only doped with Nb, ionic conductivity shows further improvement of co-doping samples. $Li_{6.7}La_3Zr_{1.5}Nb_{0.4}Sm_{0.1}O_{12}$ exhibits the highest conductivity of 1.06×10^{-3} S/cm at 30 °C, which is about twice higher than LLZO that only doped with Nb according to previous reports [26].

Based on all the above results, strong correlations among chemical composition, sinterability, and conductivity can be found. The Nb–Sm co-doping shows that it can stabilize the cubic phase structure, decrease the amount of pores, and increase the grain size, and therefore enhance sinterability and increase density, leading to lower impedance and higher conductivity.

The dependence of conductivity on temperature is shown in Fig. 6. The impedance spectra of $Li_{6.7}La_3Zr_{1.5}Nb_{0.4}Sm_{0.1}O_{12}$ measured with temperatures ranging from 30 to 120 °C are shown in Fig. 6a. The highest total conductivity of $Li_{6.7}La_3Zr_{1.5}Nb_{0.4}Sm_{0.1}O_{12}$ reaches 4.14×10^{-2} S/cm at 120 °C, significantly higher than that of 1.06×10^{-3} S/cm at 30 °C. Therefore, ionic conductivity is affected by temperature, indicating that higher ionic conductivity can be obtained when testing temperature is increased. The Arrhenius plots for temperature dependence for total ionic conductivity of $Li_{7-x+y}La_3Zr_{2-x-y}Nb_xSm_yO_{12}$ ($0 \le x \le 0.4$, $0 \le y \le 0.1$) electrolytes are shown in Fig. 6b and c. The $\log_{10}(\sigma)$ varies linearly with the reciprocal of temperature, indicating the thermally activate nature of Li conductivity. The activation energy (Ea) for lithium ion conductivity listed in Table 2 is calculated using the Arrhenius equation: $\delta_{total}T=A\exp(-Ea/k_bT)$, where A is the pre-exponential factor and k_b represents the Boltzmann constant. The activation energy of $Li_{6.7}La_3Zr_{1.5}Nb_{0.4}Sm_{0.1}O_{12}$ ceramic electrolyte is found to be 0.39 eV, which is consistent with the previous reports [27].

Figure 7 shows the DC potentiostatic polarization currents of $Li_{6.7}La_3Zr_{1.5}Nb_{0.4}Sm_{0.1}O_{12}$. The electronic conductivity of samples can be written as $\sigma_e=(I\cdot L)/(U\cdot A)$, where I is the steady current, L is the thickness of samples, U is the applied voltage (0.1 V), and A is the area of samples. Following polarization for 4000 s under DC bias voltage, electronic current achieved stability at 2.08×10^{-10} A. As a result, electronic conductivity of $Li_{6.7}La_3Zr_{1.5}N_{b0.4}Sm_{0.1}O_{12}$ is 8.60×10^{-10} S/cm, which is obviously lower than ion conductivity. Although electronic conductivity of $Li_{6.7}La_3Zr_{1.5}Nb_{0.4}Sm_{0.1}O_{12}$ is relatively low, the lowest conductivity is seen in $Li_{7.1}La_3Zr_{1.6}Nb_{0.3}O_{12}$ at 4.23×10^{-10} S/cm. The electronic conductivity is in the range of 10^{-10} to 10^{-8} S/cm for nearly all of the samples, negligible electronic conductivity indicating dominant ionic conduction in LLZO ceramics.

4 Conclusion

Garnet LLZO ceramic electrolytes with relative densities of 94.31% and ionic conductivity of 1.06×10^{-3} S/cm were obtained through Nb–Sm co-doping on Zr sites. The co-doping is found to stabilize the cubic phase, enhance

sinterability, and increase density; besides, it also shows fewer pores and larger grain size in the co-doping samples, all of which can be beneficial for improving lithium ionic conductivity.

References

1. S. Ramakumar, C. Deviannapoorani, L. Dhivya, L.S. Shankar, R. Murugan, Prog. Mater. Sci. **88**, 325–411 (2017)
2. C.W. Wang, L. Zhang, H. Xie, G. Pastel, J.Q. Dai, Y.H. Gong, B.Y. Liu, E.D. Wachsman, L.B. Hu, Nano Energy **50**, 393–400 (2018)
3. V. Thangadurai, S. Narayanan, D. Pinzaru, Chem. Soc. Rev. **45**, 4714–4727 (2014)
4. I. Garbayo, M. Struzik, W.J. Bowman, R. Pfenninger, E. Stilp, J.L.M. Rupp, Adv. Energy Mater. **8**, 1702265 (2018)
5. H. Buschmann, S. Berendts, B. Mogwitz, J. Janek, J. Power Sources **206**, 236–244 (2012)
6. Y. Chen, E. Rangasamy, C.D.L. Cruz, C.D. Liang, K. An, J. Mater. Chem. A **3**, 22868–22876 (2015)
7. R.J. Chen, M. Huang, W.Z. Huang, Y. Shen, Y.H. Lin, C.W. Nan, Solid State Ionics **265**, 7–12 (2014)
8. L. Dhivya, R. Murugan, A.C.S. Appl, Mater. Inter. **6**, 17606–17615 (2014)
9. Y.V. Baklanova, A.P. Tyutyunnik, N.V. Tarakina, A.D. Fortes, L.G. Maksimova, D.V. Korona, T.A. Denisova, J. Power Sources **391**, 26–33 (2018)
10. Z.L. Hu, H.D. Liu, H.B. Ruan, R. Hu, Y.Y. Su, L. Zhang, Ceram. Int. **42**, 12156–12160 (2016)
11. P. Bottke, D. Rettenwander, W. Schmidt, G. Amthauer, M. Wilkening, Chem. Mater. **27**, 6571–6582 (2015)
12. L.J. Miara, S.P. Ong, Y.F. Mo, W.D. Richards, Y. Park, J.M. Lee, H.S. Lee, G. Ceder, Chem. Mater. **25**, 3048–3055 (2013)
13. M. Rawlence, I. Garbayo, S. Buecheler, J.L.M. Rupp, Nanoscale **8**, 14746–14753 (2016)
14. M.L. Sanjuan, A. Orera, I. Sobrados, A.F. Fuentes, J. Sanz, J. Mater. Chem. A **6**, 2708–2720 (2018)
15. Y.H. Zhang, F. Chen, J.Y. Li, L.M. Zhang, J.J. Gu, D. Zhang, K. Saito, Q.X. Guo, P. Luo, S.J. Dong, Electrochim. Acta **261**, 137–142 (2018)
16. X.S. Wang, J. Liu, R. Yin, Y.C. Xu, Y.H. Cui, L. Zhao, X.B. Yu, Mater. Lett. **231**, 43–46 (2018)
17. S.M. Hao, H. Zhang, W. Yao, J.P. Lin, J. Power Sources **393**, 128–134 (2018)
18. Y.L. Luo, X.Y. Li, H. Chen, L.C. Guo, J. Mater. Sci. **30**, 17195–17201 (2019)
19. M. Klenk, W. Lai, Phys. Chem. Chem. Phys. **17**, 8758–8768 (2015)
20. D.W. Wang, G.M. Zhong, O. Dolotko, Y.X. Li, M.J. McDonald, J.X. Mi, R.Q. Fu, Y. Yang, J. Mater. Chem. A **2**, 20271–20279 (2014)
21. J. Wakasugi, H. Munakata, K. Kanamura, H. El-Shinawi, G. Paterson, D.A. Maclaren, J. Electrochem. Soc. **164**, A1022–A1025 (2017)
22. R. Jalem, M.J.D. Rushton, W. Manalastas, M. Nakayama, T. Kasuga, J.A. Kilner, R.W. Grimes, Chem. Mater. **27**, 2821–2831 (2015)
23. Y.L. Luo, Y.L. Zhang, Q.X. Zhang, Y.F. Zheng, H. Chen, L.C. Guo, Ceram. Int. **45**, 17874–17883 (2019)
24. M.A. Huang, M. Shoji, Y. Shen, C.W. Nan, H. Munakata, J. Power Sources **261**, 206–211 (2014)
25. J.L. Gai, E.Q. Zhao, F.R. Ma, D.Y. Sun, X.D. Ma, Y.C. Jin, Q.L. Wu, Y.J. Cui, J. Eur. Ceram. Soc. **38**, 1673–1678 (2018)
26. P.C. Zhao, Y. Xiang, Y.H. Wen, M. Li, X.Y. Zhu, S.T. Zhao, Z.Q. Jin, H. Ming, G.P. Cao, J. Eur. Ceram. Soc. **16**, 5454–5462 (2018)
27. D. Pinzaru, V. Thangadurai, J. Electrochem. Soc. **161**, A2060–A2067 (2018)